2009

Localized structures in kagome lattices

KJH Law

A Saxena

PG Kevrekidis
University of Massachusetts - Amherst, kevrekid@math.umass.edu

AR Bishop

Localized structures in Kagomé lattices

K. J. H. Law,[1] Avadh Saxena,[2] P. G. Kevrekidis,[1] and A. R. Bishop[2]

[1]*Department of Mathematics and Statistics, University of Massachusetts, Amherst MA 01003-4515, USA*
[2]*Theoretical Division and Center for Nonlinear Studies, Los Alamos National Laboratory, Los Alamos, NM 87545, USA*

We investigate the existence and stability of gap vortices and multi-pole gap solitons in a Kagomé lattice with a defocusing nonlinearity both in a discrete case and in a continuum one with periodic external modulation. In particular, predictions are made based on expansion around a simple and analytically tractable anti-continuum (zero coupling) limit. These predictions are then confirmed for a continuum model of an optically-induced Kagomé lattice in a photorefractive crystal obtained by a continuous transformation of a honeycomb lattice.

PACS numbers:

I. INTRODUCTION

Recent years have seen a great deal of interest in Hamiltonian lattice and quasi-discrete systems due to their relevance as models of experiments coming from various branches of physics. An early example is that of the nonlinear optics of fabricated AlGaAs waveguide arrays [1]. The interplay of discreteness and nonlinearity there led to the emergence of numerous phenomena that have gathered considerable attention subsequently, such as Peierls-Nabarro potential barriers, diffraction and diffraction management [2] and gap solitons [3], to name just a few. See, for example, the reviews [4, 5] and references therein.

More recently, there has been growing interest within nonlinear optics in the area of optically-induced photonic lattices in photorefractive crystals such as strontium barium niobate ($Sr_xBa_{1-x}NbO_3$, commonly abbreviated SBN). The original theroetical proposal of [6] was followed quickly by experimental realizations [7, 8], and the foundation was thus set for the observation of a diverse array of novel nonlinear phenomena in this setting. Among others, these phenomena include dipole [9], multipole [10], necklace [11], gap [3] and rotary [12] solitons as well as discrete [13, 14] and gap [15] vortices, higher order Bloch modes [16], Zener tunneling [17], as well as localized modes in honeycomb [18], hexagonal [19] and quasi-crystalline [20] lattices, and Anderson localization [21] (see, e.g., the reviews [22, 23] for additional examples).

A considerable effort along these lines has been dedicated to the recently emerging area of *non-square* lattices [18, 19, 24, 25, 26, 27, 28, 29, 30, 31, 32, 33, 34, 35, 36]. Furthermore, the majority of these studies have dealt with the case of a focusing non-linearity rather than a defocusing one. Coherent structures in the latter case have received relatively limited attention until very recently, for example in the study of fundamental and higher order gap solitons [7]. More complicated gap structures, such as multipoles and complex valued vortices are only starting to be explored in square lattices [37, 38]. A theoretical framework has been developed in parallel to this work, stemming from one-dimensional and square lattices [39, 40]. However, the predictions of the latter can also be translated to contours (or paths) in non-square geometries [29, 31], based on arguments of dimensionality reduction along the contour.

In this work we will focus on the so-called *Kagomé* lattice, which is encountered often in nature and has a very rich structure. In the solid-state community and other areas of physics and science these lattices and many others have been explored for decades [41], but are becoming more prevalent recently [42, 43]. Furthermore, low temperature properties of atomic quantum (ultracold Bose and Fermi) gases have been studied in the trimerized Kagomé lattice [41].

Motivated by recent advances in optically-induced lattices in SBN, we will explore a Non-linear Schrödinger (NLS) model in both its discrete (DNLS) manifestation as a set of difference equations adhering to the symmetry of the lattice and modeling coupled oscillators, and in the analogous continuum setting using a partial differential equation with an external potential having the appropriate symmetry. In particular, since the continuum model is motivated by experiments with SBN, the nonlinearity will be *saturable* [22, 23]. We will investigate prototypical contours (or paths) of localized structures in this lattice, consisting of six sites as well as four sites, and being both real, and complex valued with continuous phase (modulo 2π).

Our main findings in what follows are that

- Certain structures are stable, such as the in-phase gap hexapole and single-charge six-site gap vortex on the honeycomb cell, and the in-phase/out-of-phase quadrupole on the "hourglass cell" (see Fig. 1). Other configurations are unstable.

- In the continuum model, continuations of solutions in the first band-gap pass through the second band as quasi-localized structures and then become fully extended in the second band-gap. However, discontinuous extensions, i.e. new continuations of the localized structures, are found to exist in the second band-gap simultaneously with the extended states.

- The result of the evolution of the dynamical instability in these lattices is more complex than in the square lattice case, and may involve not only degeneration to single-site solitons but possibly to multi-site solitary wave structures, and, in the discrete case, often the formation of robust breathing states, consisting of multiple sites (possibly even as many as in the original configuration). In fact, we have found some clear breather formations recurring in multiple simulations:
  - Two nearest-neighbor or opposite sites in-phase with each other and with oscillating amplitudes of comparable magnitude.
  - Two next-nearest-neighbor sites out-of-phase with each other and with oscillating amplitudes of comparable magnitude.
  - Two nearest-neighbor sites having different amplitudes and oscillating between the same phases and opposite phases depending on whether the amplitudes are further from or closer to each other, respectively.

  And, in the continuum version, either all or most of the initially populated wells remain populated for long propagation distances, with the instability manifesting itself only as phase reshaping.

The presentation will be structured as follows. In section II we provide the setup of the problem, the background and the theory. Then in section III we will systematically explore the relevant numerical results. Finally, in section IV we will summarize our findings and present our conclusions.

II. SETUP

The description of the setup of the problem, including the background and theory is organized into three sections: first, the preliminary material II A; second the existence considerations II B; and third the stability considerations II C.

A. Preliminaries

We introduce the following complex-valued non-linear evolution equation

$$-iU_z = [\mathcal{L} + \mathcal{N}(\mathbf{x}, |U|^2)]U, \tag{1}$$

where U is a function of $z \in \mathbb{R}_+$ and $\mathbf{x} \in \mathbb{Z} \times \mathbb{Z}$ in the discrete version or else $\mathbf{x} \in \mathbb{R} \times \mathbb{R}$ in the continuum version. First, we will consider the discrete version with

$$\mathcal{L} = \epsilon \left(\sum_{j \in \{\pm J\}} \mathbf{e}_j - 4 \right), \tag{2}$$

where $\mathbf{e}_J$ is a translation by one site in the positive direction along J and J is one of a site-dependent subset of two of the principal lattice vectors $\mathbf{a}_d = (1, \sqrt{3})/2$, $\mathbf{b}_d = (-1, \sqrt{3})/2$, or $\mathbf{c}_d = (1, 0)$ of the discrete Kagomé lattice presented in Fig. 1 and ϵ is the coupling between sites. The non-linear term is taken to be a cubic Kerr non-linearity as follows

$$\mathcal{N}(\mathbf{x}, |U|^2) = -|U|^2. \tag{3}$$

The simulations for the static results in the discrete model were performed in the domain $D_h \backslash K$, where $D_h = [1, \ldots, 33] \times [1, \ldots, 33]$ is the discrete lattice domain corresponding to a triangular lattice and $K = \{(2m+1, 2n+1) | (m, n) \in [0, 16]^2\}$. For dynamical evolution, the solutions were buffered with 40 (or more) nodes on all sides to prevent radiation scattering from the boundaries.

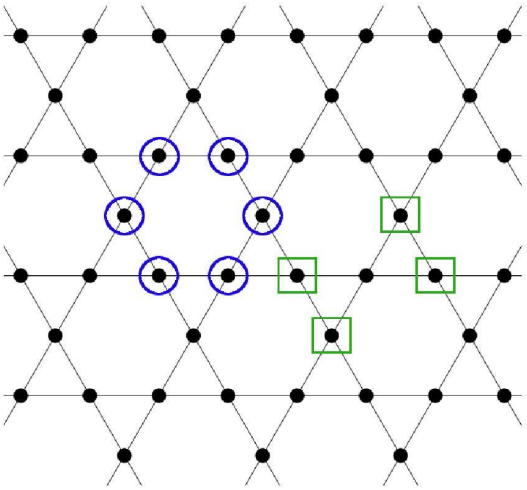

FIG. 1: (Color online) The discrete Kagomé lattice structure is presented above. The six-site contour is given by the blue circles, while the four-site "hourglass" contour is given by the green squares.

The continuum version consists of defining $\mathcal{L} = D\nabla^2$, where ∇^2 is the two-dimensional Laplacian on $\mathbb{R} \times \mathbb{R}$ and

$$\mathcal{N}(\mathbf{x}, |U|^2) = \frac{E_0}{1 + I(\mathbf{x}) + |U|^2}, \tag{4}$$

with

$$I(\mathbf{x}) = I_0 \left| f_1(\mathbf{x}) e^{ik\mathbf{b}_1 \cdot \mathbf{x}} + e^{ik\mathbf{b}_2 \cdot \mathbf{x}} + e^{ik\mathbf{b}_3 \cdot \mathbf{x}} \right|^2 \tag{5}$$

the optical lattice intensity function formed by three (p=0) or four laser beams with $f_1(\mathbf{x}) = e^{ikpx/(1+4p/3)} \cos[pkx/(1+4p/3)]$, $\mathbf{b}_1 = (1/(1+4p/3), 0)$, $\mathbf{b}_2 = (-\frac{1}{2(1+4p/3)}, -\frac{\sqrt{3}}{2})$, $\mathbf{b}_3 = (-\frac{1}{2(1+4p/3)}, \frac{\sqrt{3}}{2})$. As

$p \to 3/2$ the lattice transforms from the well-known honeycomb interference pattern into the richer Kagomé lattice. The latter lattice features both the hexagons from the honeycomb lattice and the equilateral triangles from the triangular one, and each node has four neighbors similar to the square lattice.

Here I_0 is the lattice peak intensity, z is the propagation constant and $\mathbf{x} = (x, y)$ are transverse distances (normalized to $z_s = 1$ mm and $x_s = y_s = 1\mu$m), E_0 is proportional to the applied DC field voltage, $D = z_s\lambda/(4\pi n_e x_s y_s)$ is the diffraction coefficient, λ is the wavelength of the laser in a vacuum, $d = 4\pi/k$ is the periodicity in the x-direction ($d/\sqrt{3}$ is the periodicity in the y-direction) and n_e is the refractive index along the extraordinary axis. We choose the lattice intensity $I_0 = 1$, and (d, E_0, λ, n_e)=(90,8,532 nm,2.35), consistent with a typical experimentally accessible situation [34, 37]. A plot of the potential intensity field created by the optical lattice is shown in Fig. 2 to illustrate the locations where our localized configurations will live. The non-dimensional value $D = 18.01$, and we note that this dispersion coefficient is equivalent to rescaling space by a factor $\sqrt{D}$ as, e.g. in [46].

The numerical simulations are performed in a rectangular 120×120 grid corresponding to the domain size $4d \times 8d/\sqrt{3}$ (i.e. four periods of the lattice in each direction), using a rectangular spatial mesh with $\Delta x = 1.5$ and $\Delta y \approx 1.732$. Regarding the typical dynamics of a solution when it is unstable, we simulate the z-dependent evolution using a Runge-Kutta fourth-order scheme with a step size $\Delta z = 0.01$.

B. Existence considerations

Assuming a stationary state u exists, and letting the propagation constant $-\mu$ represent the (nonlinear) real eigenvalue of the operator of the right-hand-side of Eq. (1), the corresponding eigenvector u is a fixed point of

$$[\mu + \mathcal{L} + \mathcal{N}(\mathbf{x}, |u|^2)]u = 0. \tag{6}$$

In the discrete case, we performed a continuation in ϵ. In particular, if one indexes the sites by (m, n), then solutions in the limit $\epsilon \to 0$ can easily be found of the general form $u_{m,n} = \sqrt{\mu}\exp\{-i(\mu t - \theta_{m,n})\}$ for any arbitrary $\theta_{m,n} \in [0, 2\pi)$ [40]. We can linearize Eq. (6) around the solution for $\epsilon = 0$ denoted by u_0, accounting for complex valued perturbations by considering the conjugate of Eq. (6) as well, which has the solution u_0^*. The *Jacobian* of (6) for $\varepsilon = 0$, or equivalently, in the absence of $\mathcal{L}$, is

$$\mathcal{J}(u) = [\mu + \partial(\mathcal{N}u, [\mathcal{N}u]^*)/\partial(u, u^*)].. \tag{7}$$

We may also take the coupling ε, when sufficiently small, as the small parameter in the expansion with

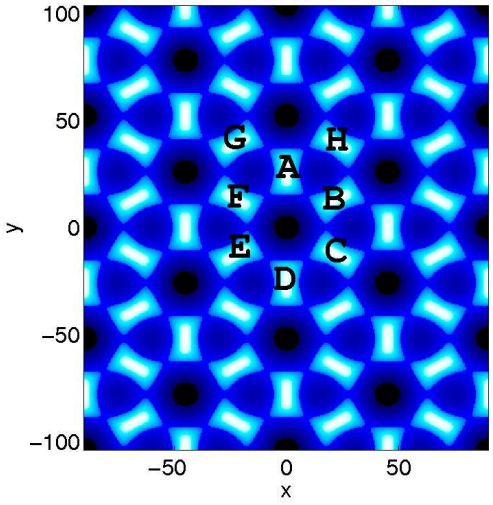

FIG. 2: (Color online) A spatial (x-y) contour plot of the effective potential created by the ordinary polarization standing wave [lattice beam in Eq. (5)]. Points A, B, C, D, E, F, G and H define the relevant potential minima for the various configurations we will consider. The contour $\{A, B, C, D, E, F\}$ is the honeycomb cell, which can be considered to tile part of the lattice. The set of sites $\{B, F, G, H\}$ comprise the "hourglass" cell contour we will consider. Together with A, these sites comprise another cell which tiles the remaining part of the lattice.

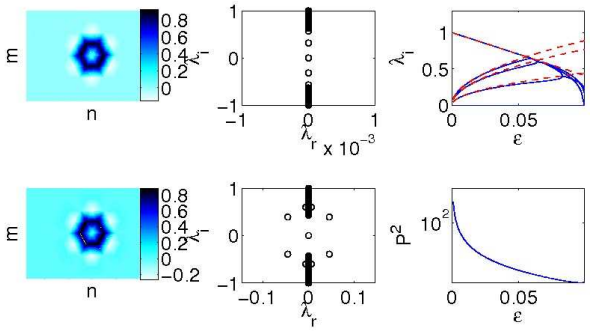

FIG. 3: (Color online) The discrete in-phase hexapole solutions are presented. In the first two columns the profiles (left) and linearization spectra are given before (top, $\epsilon = 0.061$) and after ($\epsilon = 0.085$) the first Hamiltonian Hopf (HH) bifurcation. The top right panel depicts the theoretical predictions of the linearization eigenvalues bifurcating from the AC limit (dashed) as well as the actual numerically computed ones (solid). The bottom right panel is P^2 (see Eq. (10)), shown on a log scale, where we can observe the decrease in the effective power, as the coupling strength increases.

$[u, u^*]^T = [u_0, u_0^*]^T + \varepsilon u_1$. If we denote by $\mathcal{L}_\varepsilon$ the operator $\mathcal{L}$ for coupling ε, then the first order correction in ε to Eq. (6) is

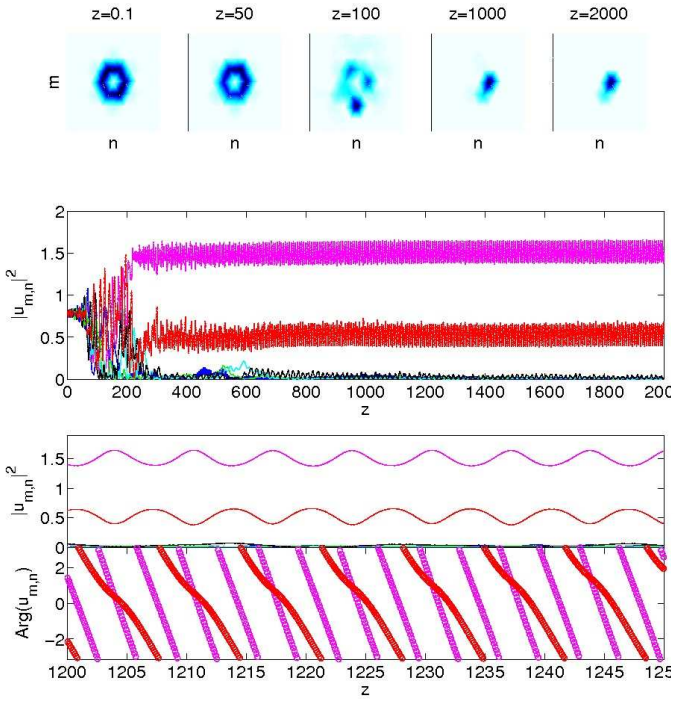

FIG. 4: (Color online) The dynamics of the solution given in the bottom row of Fig. 3 is presented. The top row shows snapshots of the modulus for various z, while the next row shows the individual amplitudes at the relevant sites. The structure survives for a while but ultimately disintegrates, due to the instability, into two populated nearest-neighboring sites whose amplitudes breathe closer and further from one another while the phases oscillate between opposite and same, respectively (see the bottom two rows).

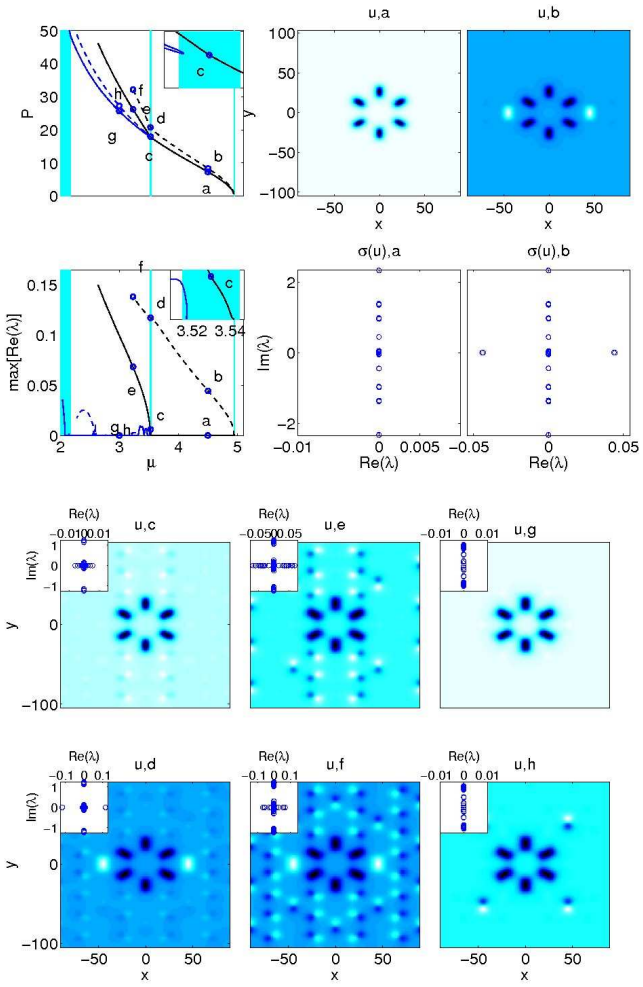

FIG. 5: (Color online) The continuum in-phase hexapole is presented in these panels. The top two left panels show the power, P (top) and instability growth rate (bottom) as given by the maximum real part of the linearization spectrum. The first band is given to the right, beyond which is the semi-infinite gap (it is displayed wider than it actually is for visibility, because its actual width is narrower than a pixel at this scale), the second band is in the middle, and the third band is at the far left. The blue branches in the second gap are actually discontinuous extensions of the localized modes from the first gap, which collide in a saddle-node bifurcation and disappear as can be observed in the inset panels in the upper right corners (this is consistent throughout the following images, but the closeups will not be shown). Solutions marked on these plots with the letters a,b,c,d,e,f,g and h are presented in the remaining panels. The second and third columns of the top set display the principal two solutions a and b, respectively, with full panels of their linearization spectra below them. The bottom six panels have miniature sub-panels with the corresponding spectra embedded in them. There are stable first (a), and also second (g and h) gap soliton structures. The solitons (c,d), with energy in the second band, are unstable.

$$\mathcal{J}(u_0)u_1 + \tfrac{1}{\varepsilon}\begin{pmatrix}\mathcal{L}_\varepsilon & 0\\ 0 & \mathcal{L}_\varepsilon\end{pmatrix}\begin{pmatrix}u_0\\ u_0^*\end{pmatrix} = 0.$$

Projecting this map onto the kernel of $\mathcal{J}(u_0)$ eliminates the first term and we are left with the condition

$$\left\langle \begin{pmatrix}\mathcal{L}_\varepsilon & 0\\ 0 & \mathcal{L}_\varepsilon\end{pmatrix}\begin{pmatrix}u_0\\ u_0^*\end{pmatrix}, \ker\{\mathcal{J}(u_0)\}\right\rangle = 0,$$

where we use $\langle\cdot,\cdot\rangle$ the standard inner product on the Hilbert space l^2. We let $\mu = 1$ without loss of generality and denote by j the indices (m,n) along the one-dimensional contour. The non-trivial part of the Jacobian $\mathcal{J}(u_0)$ decouples into a direct sum of N 2×2 blocks if there are N excited sites in the contour. For each j there is a nontrivial element $(e^{i\theta_j}, -e^{-i\theta_j})^T \in \ker\{\mathcal{J}_j(u_0)\}$. So, the condition for existence of solutions to Eq. (6) with $\varepsilon > 0$ reduces to the vanishing of the vector function $\mathbf{g}(\boldsymbol{\theta})$ of the phase vector $\boldsymbol{\theta} = (\theta_1, \ldots, \theta_N)$ where

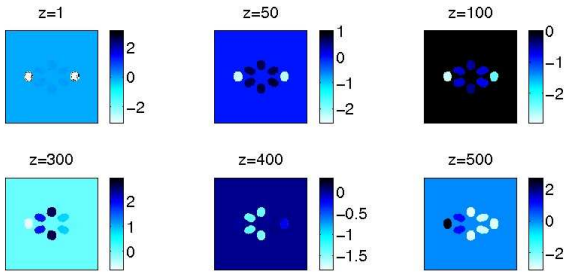

FIG. 6: (Color online) The evolution of the unstable solution given in Fig. 5 (b) is shown. The phase is shown as $\arg(u)\chi\{(x,y)||u|^2 > 0.5\max_{(x,y)}[|u|^2]\}$ at various times because the original configuration is preserved for a very long propagation distance (χ is the indicator function which annihilates the field outside of the set on which it is defined). The relative phases of the configuration break up after $z = 100$.

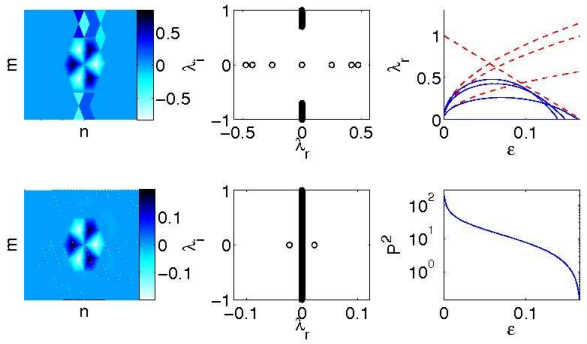

FIG. 7: (Color online) The same panels as Fig. 3 except for the unstable out-of-phase hexapole. The top row solution is for $\varepsilon = 0.05$, while the bottom one is for $\varepsilon = 0.16$.

$$g_j \equiv -\sin(\theta_j - \theta_{j-1}) - \sin(\theta_j - \theta_{j+1}), \tag{8}$$

subject to periodic boundary conditions. We consider primarily contours M within the subcategory of those for which $|\theta_{j+1} - \theta_j| = \Delta\theta$ is constant for all $j \in M$, $|\theta_1 - \theta_{|M|}| = \Delta\theta$ and $\Delta\theta|M| = 0 \bmod 2\pi$. A standard Newton fixed-point solver is used to construct branches of solutions to Eq. (6) in ε from the AC limit.

For the continuum problem where $\mathbf{x} \in \mathbb{R}^2$, there exists no such analytical solution from which to construct a continuation. On the other hand, it is well-known that localized solutions exist for values of the propagation constant μ in the complement of the linear spectrum (ie. the so-called spectral gap) defined by the following eigenvalue problem (also known as the linearization around the zero solution),

$$[\mu - \mathcal{L} - \mathcal{N}(\mathbf{x}, 0)]u = 0. \tag{9}$$

These solutions are exponentially localized in space, so-called gap-soliton, states of the original nonlinear partial differential equation. Since the parameter of interest is μ, diagnostics are plotted against μ. Continuations in this parameter can be found with a fixed-point solver and an initial guess of a collection of Gaussian wave-packets in the appropriate configuration. Using a standard eigenvalue solver package implemented through MATLAB, we identified the first two spectral gaps for our given parameters and grid size to be $G_1 \approx (3.545, 4.9454)$ and $G_2 \approx (2.178, 3.515)$. It is worth noting that the bands and gaps remain very close to the same widths for much smaller discretizations (ie. much larger grids). For instance, with 300 nodes in each direction we have $\tilde{G}_2 = (2.125, 3.463)$, so the change in width of the bandgaps is an order of magnitude closer to convergence than the position (modulo translation). We use the bands appropriate to the discretization in order to compare them with the bifurcation structure of solutions.

The localized states u of the continuum version of (6) were obtained using the Newton-Krylov fixed point solver nsoli from [47], which utilizes a GMRES iterative algorithm, based on residual reduction in successive Krylov subspaces, in order to minimize the memory necessary for the linear solver within each step of the Newton algorithm. Some care has to be taken to handle the large size of the representation of a 2D continuum domain. A pseudo-arclength continuation [48] was used to follow each branch and locate the bifurcations which occur at the edges of the bands.

The square root of the optical power of the localized waves is defined as follows:

$$P = \left[\int |U|^2 \, dS\right]^{1/2}, \tag{10}$$

where in the continuum problem, $dS = dxdy$, while in the discrete problem we define the corrsponding sum (divided by $\sqrt{\varepsilon}$).

C. Stability considerations

Stability is examined by linearizing Eq. (1) and its conjugate around an exact stationary solution $(u, u^*)^T$ to Eq. (6). If we assume the perturbation is separable of the form $\tilde{u} = e^{\lambda t} w(x)$, then we have the following eigenvalue problem for $i\lambda$

$$\left\{ i\lambda I_2 + \begin{pmatrix} I & 0 \\ 0 & -I \end{pmatrix} [\mathcal{J}(u) + \mathcal{L}_2] \right\} v = 0, \tag{11}$$

where $\mathcal{J}$ is defined in Eq. (7) and $\mathcal{L}_2, I_2$ are the 2×2 block diagonal matrices with $\mathcal{L}, I$ (respectively) on the diagonal. The eigenvalue problem imposes no restriction on

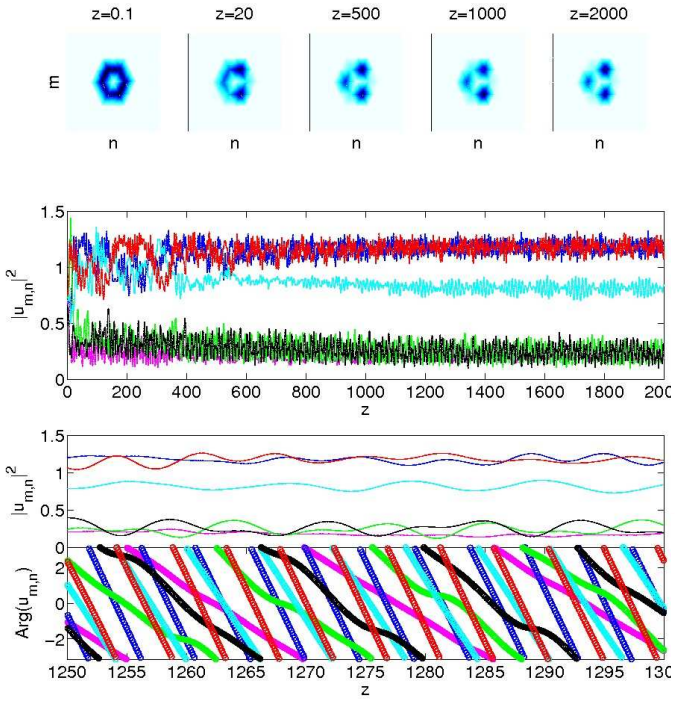

FIG. 8: (Color online) The same as Fig. 4 for the out-of-phase solution given in the top row of Fig. 7. The original configuration clearly shifts very rapidly, although the different sites remain populated for a long propagation distance. The largest amplitude pair which is separated by one node (i.e. next-nearest neighbors) remains very close to exactly out-of-phase, while the next smallest, which is also next-nearest neighbor to both, passes from the phase of one to the other. The other three sites do not exhibit any phase correlation, although at times two have matching phase and are out-of-phase with the other.

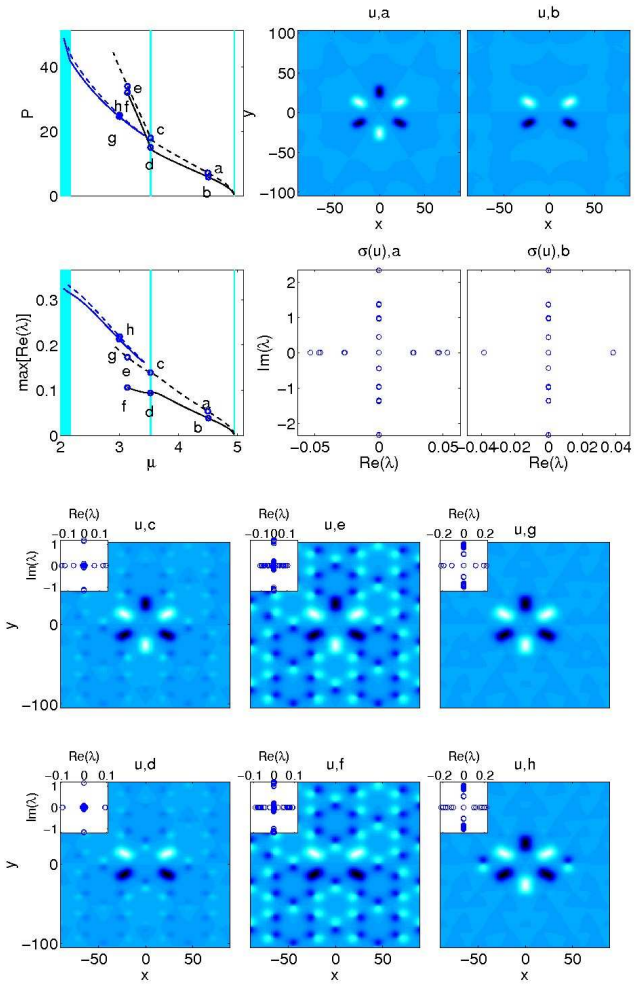

FIG. 9: (Color online) The same panels as Fig. 5, but for the out-of-phase hexapole.

the eigenvectors v. This form of the Jacobian is identical for the discrete and continuum versions of the problem, up to the definitions of the operators $\mathcal{N}$ and $\mathcal{L}$ and the domain in which the spatial variables live. The modest size of this matrix for the discrete case, $[2 \times 33 \times 33]^2$ is not a problem for a full diagonalization and we implement the MATLAB function **eig** to do so. On the other hand, the matrix for the model of the continuous domain is $[2 \times 120 \times 120]^2$ and cannot be inverted. Fortunately a standard finite difference discretization leads to a sparse banded matrix which is perfectly suited for Arnoldi iterative algorithms which minimize memory and use successive approximations of eigenvalues and eigenvectors until convergence. Such a method is implemented by the MATLAB function **eigs**, which we use here.

Twofold symmetry over each of the real and imaginary axes is guaranteed by the fact that the Jacobian of the full problem, which defines the linearization at any point, H has the property that $JHJ = H^T$ (where J is the canonical symplectic matrix having the properties $JJ = -I$ and $JJ^T = I$, which implies $e^H = M$ is *symplectic* or

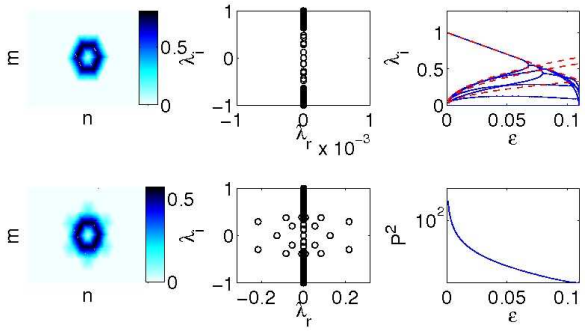

FIG. 10: (Color online) The same panels as Fig. 3 except for the stable single charge vortex solution and the modulus of the profiles are given, i.e. $|u|^2$ instead of u. The particular solutions are for $\varepsilon = 0.06$ (top) and $\varepsilon = 0.11$ (bottom).

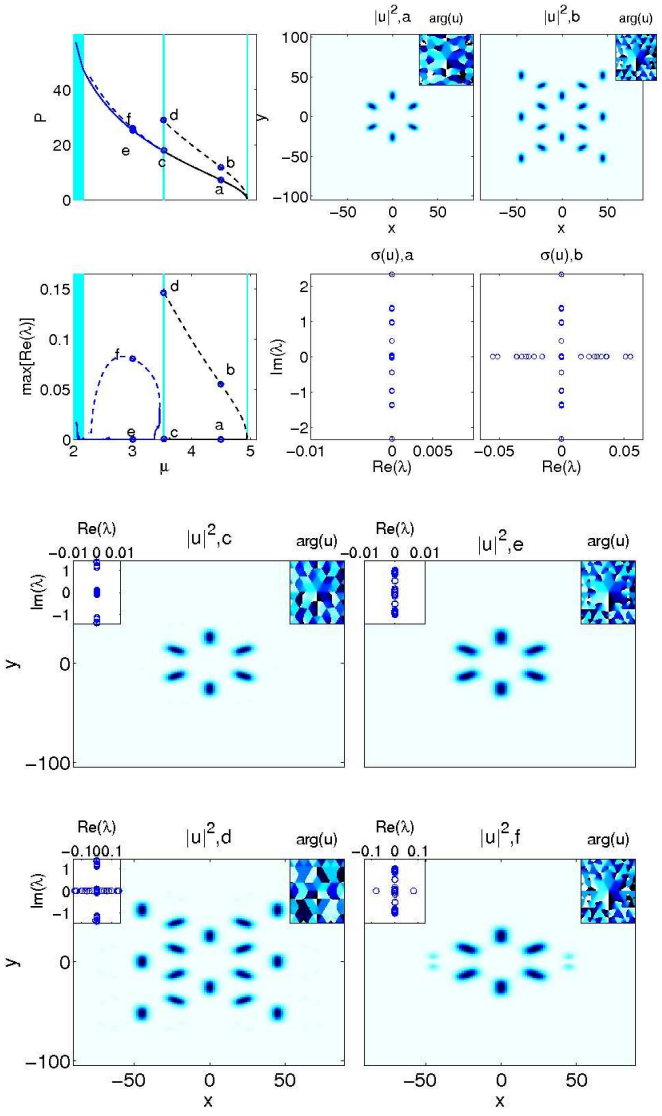

FIG. 11: (Color online) The same panels as Fig. 5, but for the single charge vortex solution and again, as in the analogous discrete case, the modulus is given in lieu of the field itself. Here there are small embedded panels in the top right corners of the profile images with the phase of the solution. Also, we were not able to identify continuations of the branches from the first gap into extended solutions in the second gap in this case, although we did identify semi-extended states.

$M^T J M = J$), and so $\mathrm{Re}(\lambda_j) \neq 0$ implies an instability.

In the discrete case, the stability will be compared to analytical results for small ε based on Lyapunov-Schmidt analysis of the expansion of the equation around the AC limit (see, e.g. [40] and references therein for details). For the contour M, there are $|M|$ eigenvalues γ_j of the $|M| \times |M|$ Jacobian $\mathcal{M}_{jk} = \partial g_j / \partial \theta_k$ of the diffeomorphism given in Eq. (8). Now, for each excited site, there are a zero and a negative eigenvalue of $\{\mathcal{J}(u_0)\}$, which are both mapped to zero eigenvalues of $\begin{pmatrix} I & 0 \\ 0 & -I \end{pmatrix}\{\mathcal{J}(u_0)\}$. So, one can follow the same procedure for the eigenvalue problem of the linearization (Eq. 11) of the original problem, except projecting also onto the generalized kernel and expanding to lower order ($\sqrt{\varepsilon}$) and, hence, obtain a mapping between its eigenvalues and those of the Jacobian of $\mathbf{g}$. In particular, for each eigenvalue γ_j of $\mathcal{M}$, the full linearization around a stationary solution with non-zero nodes in M, given by Eq. (11), will have an eigenvalue pair λ_j given, to leading order, by $\lambda_j = \pm\sqrt{2\gamma_j \varepsilon}$ in the case that the sites in M are nearest neighbors of each other. If the excited nodes are separated by a site then, for the DNLS model eigenvalues, ε is replaced by ε^2 in the previous relation. The Jacobian matrix $\mathcal{M}$ has the following form:

$$(\mathcal{M})_{j,k} = \begin{cases} -\cos(\theta_{j+1} - \theta_j) - \cos(\theta_{j-1} - \theta_j), & j = k, \\ \cos(\theta_j - \theta_k), & j = k \pm 1, \\ 0, & |k - j| \geq 2. \end{cases} \quad (12)$$

We now briefly discuss the principal stability conclusions, for the defocusing case of [29, 39], which we expect to remain valid in the present configuration. Nearest neighbor excitations in the defocusing case correspond to nearest neighbor excitations in the focusing case, but with an additional π phase in the relative phase of the sites added by the so-called staggering transformation [39]. Therefore, the in-phase nearest neighbor configuration in the defocusing case corresponds to an out-of-phase such configuration in the focusing case (and should thus be stable) [40]. On the other hand, next nearest neighbor out-of-phase defocusing configurations would correspond to next nearest neighbor out-of-phase focusing configurations and should also be stable (at least in some parameter regimes). By the same token, out-of-phase nearest neighbor, and in-phase next nearest neighbor structures should be unstable. Finally, the single-charge vortex and in-phase hexapoles should be stable, while the double charge vortex and out-of-phase hexapoles should be unstable. However, notice that, as discussed in [39], the multipole structures characterized as potentially stable above will, in fact, typically possess imaginary eigenvalues of negative Krein signature (see e.g. [49] and references therein). These may lead to oscillatory instabilities through complex quartets of eigenvalues, which arise by means of Hamiltonian-Hopf (HH) bifurcations [50] emerging from collisions with eigenvalues of opposite (i.e., positive) Krein signature. These conclusions will be discussed in connection with our detailed numerical results in what follows.

III. NUMERICAL RESULTS

Now, the above theoretical predictions will be matched against systematic numerical simulations. First, for the discrete model, we will perform continuations in the coupling parameter from the AC limit in order to compare the resulting relevant eigenvalues from the linearization spectrum with the corresponding prediction. Next, we will test these results against the continuum model. The stability results from the discrete case are expected to hold in the sense that there will either be real eigenvalue pairs in the spectrum of the solutions whose discrete analog is unstable close to the AC limit, or else there will be intervals of stability and quartets of eigenvalues due to HH and inverse HH bifurcations. The continuum model reveals not only gap soliton solutions in both the first and the second gaps, but also solitons from where the branch of solutions from the first gap passes through the first band and subsequently becomes extended. Unstable solutions were evolved in time in order to observe their dynamical behavior. Most solutions in the discrete case decompose into breathing configurations with fewer populated sites and some interesting phase correlations. In the continuum case, most configurations survive for a long propagation distance, with instabilities manifested only as phase reshaping.

This section will be composed of two parts, the first of which will address configurations with six neighbors on the hexagonal cell, the results of which are consistent with recent results in the continuum honeycomb defocusing case [29] and both honeycomb and hexagonal [31] focusing cases (translated with the appropriate staggering transform along the contour). In the second part we will look at quadrupoles along the four corners of the "hourglass" cell which is unique to the Kagomé lattice.

A. Vortices and hexapoles in the hexagonal cell

The results for the six-site configurations in the hexagonal cell are presented in this section. First we will consider the real-valued configurations of $\Delta\theta = 0$ and $\Delta\theta = \pi$ and then the complex-valued ones where $\Delta\theta = \pi/3$ and $\Delta\theta = 2\pi/3$.

1. In-phase

Here we will consider the results of the predictions from the previous section for the six-site in-phase configuration (i.e. $\Delta\theta = 0$). This configuration has been predicted to be *stable*. In the discrete model close to the AC limit, Eq. 12 predicts, to first order in ε, two double pairs of eigenvalues $i\sqrt{2\varepsilon}, i\sqrt{6\varepsilon}$ and single pairs at $i\sqrt{8\varepsilon}$ and 0. Here we digress slightly to discuss the bound of the phonon band. We consider plane waves of the form $w = e^{i(pn+qm)}$, in each of 2 (of the 3) principal directions, which are used to index the 2-dimensional lattice [28], (m, n). Since there are 3 types of nodes in this case, each having neighbors in 2 of the 3 principal directions (that are the same for the hexagoinal lattice), we must consider a linear combination of equal 1/3 weights of the corresponding dispersion relation for each type. This is equivalent to 2/3 of the dispersion relation of the hexagonal lattice, i.e.

$$\mathcal{L}_\varepsilon w = (4 - \frac{4}{3}[\cos(q) + \cos(p) + \cos(p+q)])\varepsilon < 6\varepsilon. \quad (13)$$

So, the smallest eigenvalue of the phonon band is given by $i(1 - 6\varepsilon)$, and upon its collision with the eigenvalues which bifurcated from the origin, a cascade of HH bifurcations ensues. The numerical results are presented in Fig. 3. The left column displays two solutions, before (top) and after (bottom), the continuous spectrum intersects with the bifurcation eigenvalues. The middle column has the corresponding linearization spectra. The top right panel depicts the imaginary component of the bifurcation eigenvalues as given numerically (solid line) and by the first order theoretical approximation (dashed line).

The dynamical evolution of the unstable solution from the bottom row is displayed in Fig. 4. Eventually the instability manifests itself and the original configuration is destroyed. Two nearest-neighbor sites remain with different amplitudes that oscillate. When they are closer in amplitude they are out-of-phase while when they are further apart, they are in-phase. It is worth noting here that a similar phenomenon was found in the hexagonal as well as the honeycomb lattices with a focusing nonlinearity in [31], except with the relative phases reversed, i.e. the sites were in-phase when closer and out-of-phase when further apart, presumably due to the nature of the nonlinearity (focusing versus the defocusing one here).

Next we investigate the in-phase hexapole in the continuum setting. The solution is stable in the entire first band-gap (see Fig. 5, top two rows and *a*). When it reaches the first band it collides with an unstable branch (b) which has two neighboring wells populated out-of-phase and disappears in a saddle-node bifurcation. When these branches reach the second band, they immediately become unstable as they reshape into extended solutions (see e,f). There does exist a second-gap soliton solution which is stable, (g). This solution disappears in a saddle-node bifurcation with a marginally stable solution that has next-nearest-neighbor wells on four sides populated with intra-site dipoles. The evolution of solution (b) is represented in Fig. 6 by the phase of the sites via the following quantity $\arg(u)\chi\{(x,y)||u|^2 > 0.5\max_{(x,y)}[|u|^2]\}$, where χ is the indicator function of the set that annihilates the field outside that set. All sites remain for a long propagation distance, although the phase correlation is lost by $z = 300$.

2. Out-of-phase

In this section, we consider the *unstable* out-of-phase hexapole ($\Delta\theta = \pi$). First, in the discrete case presented in Fig. 7 the theoretical prediction of linearization eigenvalues, which are exactly a factor $-i$ times those for the in-phase solution, are confirmed for small ε. The dashed line $1 - 6\varepsilon$, which represents the smallest phonon eigenvalue, is included here to show that the actual linearization eigenvalues remain bounded by this line, similarly to what was observed for square lattices in [39]. A solution is shown for small coupling and large gap, as well as one when the gap is closing and the solution decaying. The dynamics in Fig. 8 reveal that all sites survive for a long propagation distance, and, while there is no clear phase correlation between all sites, there is between some. For instance, the largest amplitude two next-nearest-neighbor lobes remain out-of-phase. This is again consistent with a feature that was recently observed in [31], since next-nearest-neighbor interactions are expected to be the same for focusing and defocusing non-linearities due to the staggering transformation [40]. The middle amplitude site next-nearest to both of these oscillates between in-phase with one and then the other, while there is no apparent correlation of the other three smaller amplitude sites.

The same panels as the in-phase case, Fig. 5, are shown for the continuum version of the out-of-phase hexapole in Fig. 9. The solution this time actually collides with a four-well structure, which is slightly more stable, due to fewer unstable pairs of populated wells. Again there are continuations through the second band to extended states and again there exists a disjoint branch of second gap states. All states here are unstable. Under dynamical evolution, again all six sites remain for a long propagation distance (not shown). However, the phase correlation breaks down as early as $z = 20$, due to the instability.

3. Single charge vortices

Next we look at the *stable* single charge vortex solution ($\Delta\theta = \pi/3$). The discrete problem is predicted to be stable with double pairs of eigenvalues at $\pm i\sqrt{\varepsilon}$ and $\pm i\sqrt{3\varepsilon}$, and single pairs at $\pm 2i\sqrt{\varepsilon}$ and 0. The prediction is confirmed in Fig. 10 and there is good agreement until the HH bifurcations set in with the continuous spectrum when $\sqrt{\varepsilon} \approx \lambda_i = 1 - 6\varepsilon$. A cascade of such bifurcations follows and an example profile and spectrum after this time are shown in the bottom left. The evolution of the unstable solution from the bottom row was investigated (not shown) and four sites decompose into essentially background radiation, while two cells opposite to one another inherit most of the power and remain close in amplitude and in-phase for a long distance. This is again in agreement with the results of [31], since in-phase opposite sites on the honeycomb cell are next-to-next-nearest-neighbors, so with a defocusing nonlinearity it is equivalent to an out-of-phase pair with a focusing nonlinearity. Many comparable amplitude out-of-phase breathers were found in [31].

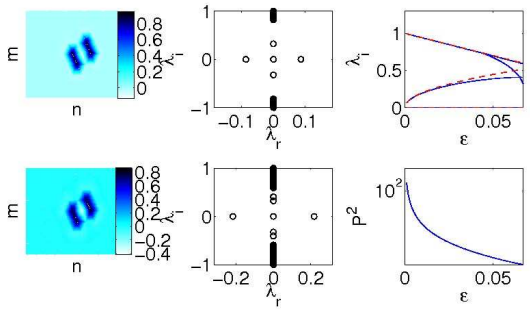

FIG. 12: (Color online) The same panels in the left two columns as Fig. 3 except for the unstable in-phase quadrupole in the hourglass cell. The particular solutions shown are for $\varepsilon = 0.03$ (top) and $\varepsilon = 0.067$ (bottom).

The continuum version of this configuration given in Fig. 11 (a) collides in a saddle-node bifurcation with an unstable configuration with additional populated sites on the perimeter, (b). The second gap version (e) collides with an unstable state (f) having two intrasite dipoles populated outside the original vortex. However, this state appears to stabilize closer to the third band. In the dynamical evolution of (b, not shown) again the original configuration of "mass" survives for a long propagation distance, while the phase correlation decomposes by $z = 100$.

4. Double-charge vortices

The last of the six-site configurations we consider is the double-charge vortex ($\Delta\theta = 2\pi/3$). The stability predictions are again confirmed for small ε; however, due to the instability of the branch throughout its existence range, we do not present the details here for the sake of brevity. The continuum model admits similar branch structure for this solution as for previous cases. Here also, the solution is unstable for all the cases examined. Its dynamics showed the principal sites surviving for long propagation distances, although the structure eventually disintigates. Again due to the generic instability of this branch, numerical details are omitted here.

B. Quadrupoles in the hourglass cell

Next, we consider configurations around the outer 4-site contour of the hourglass cell. Now, in this case, the five sites comprising the hourglass are not a simple curve, i.e. the curve crosses itself, and since some nodes

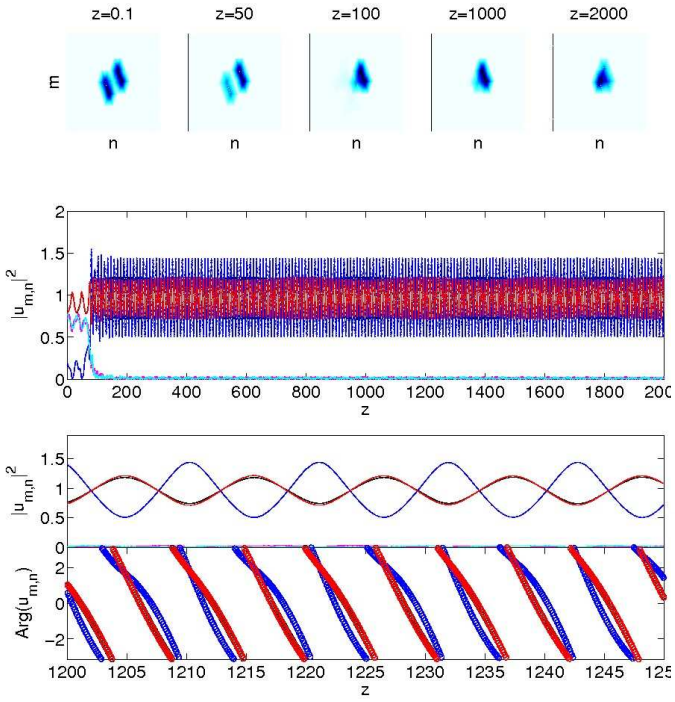

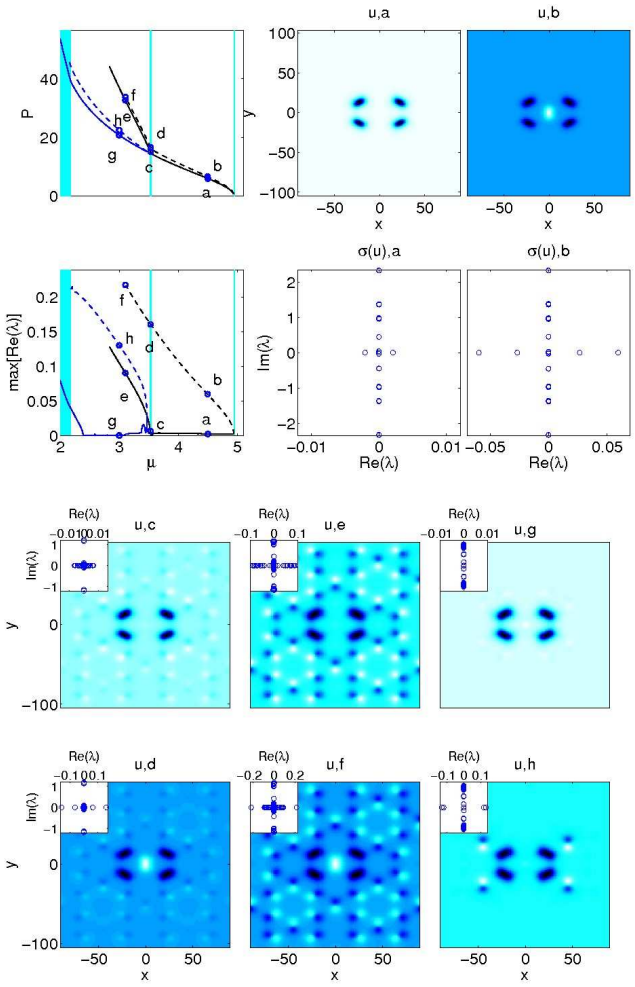

FIG. 13: (Color online) The same as Fig. 4 for the in-phase quadrupole given in the bottom row of Fig. 12. The center site becomes populated around $z = 100$ and the remaining in-phase tripole (expected to be stable) persists for a long distance with two sites almost exactly in-phase, and with equal amplitudes, while the other has much larger oscillations in amplitude opposite to the other two, but has very similar phase.

FIG. 14: (Color online) The same panels as Fig. 5, but for the in-phase quadrupole. A more unstable configuration with the center well populated out-of-phase collides with this one close to the first band-edge.

are nearest-neighbors, while others are next-nearest, the analysis must be taken to second order for accurate predictions of all the bifurcating eigenvalues. Instead, we consider only nearest neighbors analytically and extend previous results about higher-order interactions to make qualitative predictions there.

C. In-phase quadrupoles

First, we consider the in-phase quadrupole. The prediction of the discrete model to first order, i.e. for nearest neighbors, is that this configuration will have double eigenvalue pairs at $\pm 2i\sqrt{\varepsilon}$ (due to the in-phase nearest neighbors predicted to be stable). On the other hand, next-nearest neighbors which are in-phase are expected to be unstable [29, 39] and indeed a real pair does bifurcate as well. The real pair comes at higher order because it is a higher-order splitting. The results are presented in Fig. 12. The panels are the same as for Fig. 3. The evolution in Fig. 13 reveals a unique structure with three sites very close in phase and intensity, two nearly identical and one slightly different with its intensity oscillating

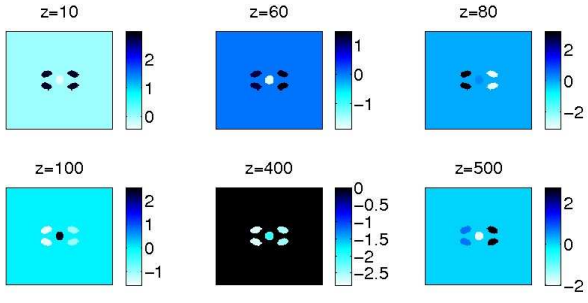

FIG. 15: (Color online) The same as Fig. 6 but for the in-phase quadrupole from Fig. 14 (b). The initial relative phase loses the correlation after $z = 60$ and the structure again persists for a long distance.

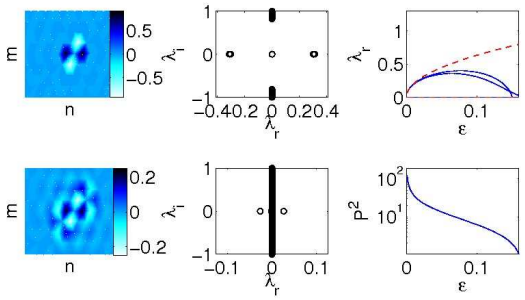

FIG. 16: (Color online) The same panels as Fig. 12 except for the unstable out-of-phase quadrupole. The particular solutions shown are for $\varepsilon = 0.03$ (top) and $\varepsilon = 0.16$ (bottom).

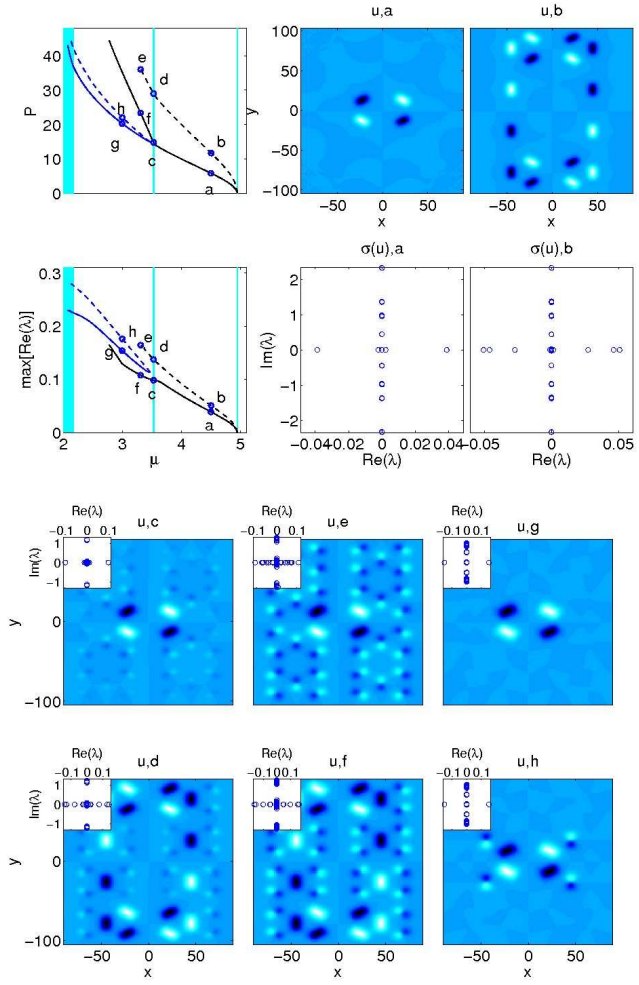

FIG. 17: (Color online) The same panels as Fig. 5, but for the out-of-phase quadrupole. It collides with a branch that has a similar phase pattern as the original configuration.

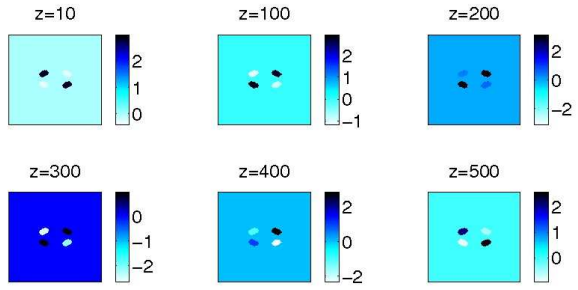

FIG. 18: (Color online) The same as Fig. 6 but for the unstable out-of-phase quadrupole given in Fig. 17 (a).

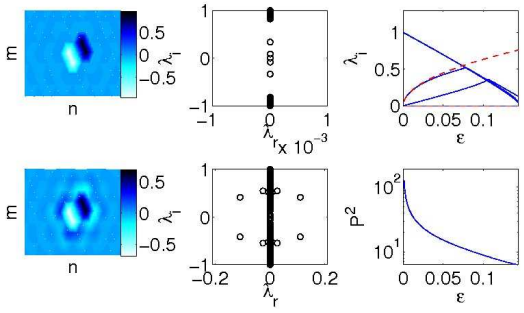

FIG. 19: (Color online) The same panels as Fig. 3 except for the stable in-phase/out-of-phase quadrupole. The particular solutions shown are for $\varepsilon = 0.03$ (top) and $\varepsilon = 0.144$ (bottom).

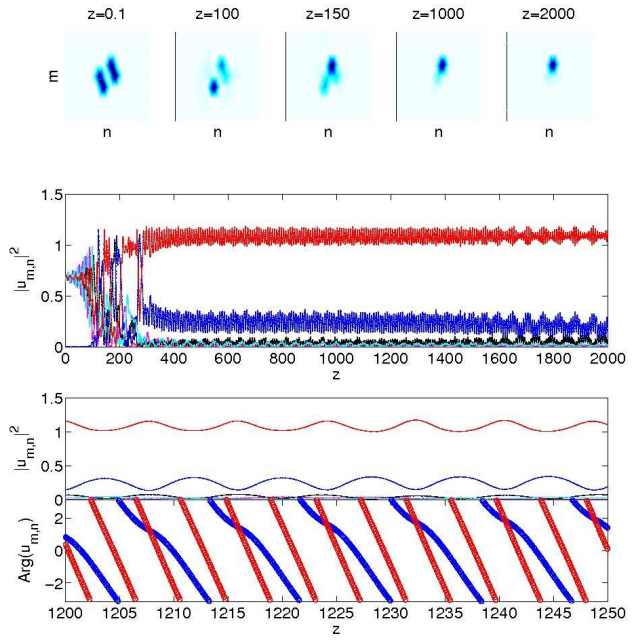

FIG. 20: (Color online) The same panels as Fig. 5, but for the in-phase/out-of-phase quadrupole.

with larger amplitude opposite to the others. One of the sites is the originally unpopulated center site, which becomes populated when the other two disintegrate around $z = 100$.

The continuum version of this configuration disappears at the first band edge when it collides with a more unstable solution having the center site populated out-of-phase to the others (see Fig. 14). The main branch is only weakly unstable from the higher order interactions and, in fact, the second-band solution actually becomes stable for $\mu \lesssim 3$. In the dynamical evolution of the structure from Fig. 14 (b), the unstable five site in-phase structure remains very robust for a long distance with reshaped phase; see Fig. 15.

D. Out-of-phase quadrupoles

Next we consider the out-of-phase quadrupole. The predicted eigenvalues are the same as those of the in-phase case, multiplied by i. They are fairly accurate for small ε as one can see in the top right panel of Fig. 16. The dynamical evolution of the solution given in the top row of Fig. 16 reveals two pairs of uneven amplitude breathers with phases and amplitudes oscillating opposite to each other as in Fig. 3 (not shown).

This solution in the continuum version, as seen in Fig. 17, is always unstable. It collides with a structure that has a similar phase pattern, but which is surrounding rather than including the original configuration. At the point of bifurcation the common structure they share is two rows of opposite phase. Again the unstable configuration persists for a long propagation distance, suffering merely a reshaping of the relative phase (see Fig. 18).

E. In-phase/Out-of-phase quadrupoles

Finally, we turn to the quadrupole solution which has its nearest-neighbors in-phase and the next-nearest ones out-of-phase. The theoretical prediction for the discrete model based on the set of all possible dipole configurations always implies stability. Indeed the precise first order calculation predicts this configuration will also be stable with two pairs of eigenvalues at $\pm i2\sqrt{\varepsilon}$. Moreover, previous results [29, 39] predict that next-nearest neighbors which are out-of-phase will be stable, and all those in this configuration (except the ones which are also nearest) are out-of-phase. The agreement is very good again as given in the top right panel of Fig. 19.

The dynamical evolution of this configuration (not shown) again reveals the usual in-phase to out-of-phase uneven intensity breather pair, as shown first in Fig. 4.

The continuum version is presented in Fig. 20. Stable first and second band versions of the solution are identified and again there are bifurcations at the first and second bands, and also intermediate as well as extended solutions. The solution that collides with the main branch at the first band-edge (b) was propagated (not shown) and again the original sites persist and the relative phase reshapes after $z = 50$.

IV. CONCLUSIONS

In conclusion, we have presented results of prototypical contours (i.e. hexagonal and "hourglass") of localized structures in a Kagomé lattice symmetry with a defocusing nonlinearity for both a discrete model and an analogous continuum model that is relevant to experiments on the nonlinear optics of photonic lattices in photorefractive crystals. We have identified stable configurations such as the in-phase hexapole and single-charge six site vortex on the honeycomb cell, as well as the four-site in-phase/out-of-phase quadrupole and the second-gap in-phase quadrupole on the hourglass cell. Many of the structures admitted not only second gap localized structures but also semi-localized structures having energy within the second band and extended structures in the second band-gap.

The unstable solutions were evolved in time and all of the discrete structures persisted, with recurring dynamical breathing configurations reappearing in several cases, such as the comparable intensity in-phase pair and the uneven oscillating intensity pair which are out-of-phase when their intensities are closer and in-phase when they are further. In the continuum model, there was very little deviation from the amplitudes of the initial configurations and instability was manifested through phase reshaping. This suggests that the Kagomé lattice is a robust structure in which to perform experiments.

This work suggests many interesting directions to pursue, the most obvious of which is the experimental realization of these structures in optical lattices in photorefractive media and ultracold atomic gases [41]. Also, the structures with energy in the second band and higher band-gaps warrant a deeper investigation, and it is conceivable that exact breather solutions could be found with structure similar to the ones that reappear in the dynamics. Beyond that, higher dimensional extensions would also be a challenging endeavor.

Acknowledgments. KJHL gratefully acknowledges the warm hospitality of the Center for Nonlinear Studies at Los Alamos National Laboratories. PGK acknowledges support from NSF-DMS-0619492, NSF-DMS-0806762, NSF-CAREER, as well as from the Alexander von Humboldt Foundation.

[1] H.S. Eisenberg, Y. Silberberg, R. Morandotti, A. R. Boyd, and J. S. Aitchison, Phys. Rev. Lett. **81**, 3383 (1998).

[2] R. Morandotti, U. Peschel, J. S. Aitchison, H. S. Eisenberg, and Y. Silberberg, Phys. Rev. Lett. **83**, 2726 (1999); H. S. Eisenberg, Y. Silberberg, R. Morandotti, and J. S. Aitchison, Phys. Rev. Lett. **85**, 1863 (2000).

[3] D. Mandelik, R. Morandotti, J. S. Aitchison, and Y. Silberberg, Phys. Rev. Lett. **92**, 093904 (2004).

[4] D. N. Christodoulides, F. Lederer, and Y. Silberberg, Nature **424**, 817 (2003); A. A. Sukhorukov, Yu. S. Kivshar, H. S. Eisenberg, and Y. Silberberg, IEEE J. Quant. Elect. **39**, 31 (2003).

[5] S. Aubry, Physica **103D**, 201 (1997); S. Flach and C. R. Willis, Phys. Rep. **295**, 181 (1998); P. G. Kevrekidis, K.Ø. Rasmussen, and A. R. Bishop, Int. J. Mod. Phys. B **15**, 2833 (2001).

[6] N. K. Efremidis, S. Sears, D. N. Christodoulides, J. W. Fleischer, and M. Segev Phys. Rev. E **66**, 46602 (2002).

[7] J. W. Fleischer, M. Segev, N. K. Efremidis, and D. N. Christodoulides, Nature **422**, 147 (2003).

[8] J. W. Fleischer, T. Carmon, M. Segev, N. K. Efremidis, and D. N. Christodoulides, Phys. Rev. Lett. **90**, 023902 (2003).

[9] J. Yang, I. Makasyuk, A. Bezryadina, and Z. Chen, Opt. Lett. **29**, 1662 (2004).

[10] J. Yang, I. Makasyuk, A. Bezryadina, and Z. Chen, Stud. Appl. Math. **113**, 389 (2004).

[11] J. Yang, I. Makasyuk, P. G. Kevrekidis, H. Martin, B. A. Malomed, D. J. Frantzeskakis, and Z. Chen, Phys. Rev. Lett. **94**, 113902 (2005).

[12] Y.V. Kartashov, V.A. Vysloukh, and L. Torner, Phys. Rev. Lett. **93**, 093904 (2004); X. Wang, Z. Chen, and P. G. Kevrekidis, Phys. Rev. Lett. **96**, 083904 (2006).

[13] D. N. Neshev, T. J. Alexander, E. A. Ostrovskaya, Yu. S. Kivshar, H. Martin, I. Makasyuk, and Z. Chen, Phys. Rev. Lett. **92**, 123903 (2004).

[14] J. W. Fleischer, G. Bartal, O. Cohen, O. Manela, M. Segev, J. Hudock, and D. N. Christodoulides, Phys. Rev. Lett. **92**, 123904 (2004).

[15] G. Bartal, O. Manela, O. Cohen, J.W. Fleischer, and M. Segev, Phys. Rev. Lett. **95**, 053904 (2005).

[16] D. Träger, R. Fischer, D.N. Neshev, A.A. Sukhorukov, C. Denz, W. Królikowski and Yu.S. Kivshar, Optics Express **14**, 1913 (2006).

[17] H. Trompeter, W. Królikowski, D.N. Neshev, A.S. Desyatnikov, A.A. Sukhorukov, Yu.S. Kivshar, T. Pertsch, U. Peschel, and F. Lederer, Phys. Rev. Lett. **96**, 053903 (2006).

[18] O. Peleg, G. Bartal. B. Freedman, O. Manela, M. Segev and D.N. Christodoulides, Phys. Rev. Lett. **98**, 103901 (2007).

[19] C.R. Rosberg, D.N. Neshev, A.A. Sukhorukov, W. Krolikowski, and Yu.S. Kivshar, Opt. Lett. **32**, 397 (2007).

[20] B. Freedman, G. Bartal, M. Segev, R. Lifshitz, D.N. Christodoulides, and J.W. Fleischer, Nature **440**, 1166 (2006).

[21] T. Schwartz, G. Bartal, S. Fishman, and M. Segev, Nature **446**, 52 (2007).

[22] J.W. Fleischer, G. Bartal, O. Cohen, T. Schwartz, O. Manela, B. Freedman, M. Segev, H. Buljan, and N. K. Efremidis, Opt. Express **13**, 1780 (2005).

[23] Z. Chen, H. Martin, E. Eugenieva, J. Xu, and J. Yang, Opt. Express **13**, 1816 (2005).

[24] See e.g., A. Szameit, Y. V. Kartashov, F. Dreisow, M. Heinrich, V. A. Vysloukh, T. Pertsch, S. Nolte, A. Tunnermann, F. Lederer, and L. Torner, Opt. Lett. **33**, 663 (2008).

[25] T.J. Alexander, A.S. Desyatnikov, and Yu.S. Kivshar, Opt. Lett. **32**, 1293 (2007).

[26] H. Sakaguchi and B. A. Malomed. Phys. Rev. E **74**, 026601 (2006).

[27] P.G. Kevrekidis, B.A. Malomed, and Yu.B. Gaididei, Phys. Rev. E **66**, 016609 (2002).

[28] V. Koukouloyannis and R.S. MacKay, J. Phys. A: Math. Gen. **38**, 1021 (2005).

[29] K.J.H. Law, H. Susanto, and P.G. Kevrekidis. Phys. Rev. A **78**, 033802 (2008).

[30] V. Koukouloyannis, P.G. Kevrekidis, I. Kourakis, D. Frantzeskakis, and K.J.H. Law, in the Proceedings of the 35th EPS Conference on Plasma Physics (2008).

[31] K.J.H. Law, P.G. Kevrekidis, V. Koukouloyannis, I. Kourakis, D.J. Frantzeskakis, and A.R. Bishop. Phys. Rev. E **78**, 066610 (2008).

[32] M.J. Ablowitz, B. Ilan, E. Schonbrun, and R. Piestun, Phys. Rev. E **74**, 035601 (2006).

[33] B. Freedman, G. Bartal, M. Segev, R. Lifshitz, D.N. Christodoulides, and J.W. Fleischer, Nature (London) **440**, 1166 (2006).

[34] C.R. Rosberg, D.N. Neshev, A.A. Sukhorukov, W. Krolikowski, and Yu.S. Kivshar, Opt. Lett. **32**, 397 (2007).

[35] T.J. Alexander, A.S. Desyatnikov, and Yu.S. Kivshar, Opt. Lett. **32**, 1293 (2007).

[36] O. Peleg, G. Bartal, B. Freedman, O. Manela, M.Segev, and D. Christodoulides, Phys. Rev. Lett. **98**, 103901 (2007).

[37] L. Tang, C. Lou, X. Wang, D. Song, X. Chen, J. Xu, Z. Chen, H. Susanto, K. Law, and P.G. Kevrekidis, Opt. Lett. **32**, 3011 (2007).

[38] D. Song, L. Tang, C. Lou, X. Wang, J. Xu, Z. Chen, H. Susanto, K.J.H. Law, and P.G. Kevrekidis. Opt. Exp. **16**, 10110 (2008).

[39] P.G. Kevrekidis, H. Susanto, and Z. Chen, Phys. Rev. E **74**, 066606 (2006).

[40] D.E. Pelinovsky, P.G. Kevrekidis, and D.J. Frantzeskakis, Physica D **212**, 1 (2005); *ibid* **212**, 20 (2005).

[41] L. Santos, M.A. Baranov, J.I. Cirac, H.-U. Everts, H. Fehrmann, and M. Lewenstein, Phys. Rev. Lett. **93**, 030601 (2004); B. Dmaski, H.-U. Everts, A. Honecker, H. Fehrmann, L. Santos, and M. Lewenstein, Phys. Rev. Lett. **95**, 060403 (2005); B. Damski, H. Fehrmann, H.-U. Everts, M. Baranov, L. Santos, and M. Lewenstein, Phys. Rev. A **72**, 053612 (2005).

[42] R.G. Hutchinson and N.A. Fleck. J. Mech. and Phys. Sol. **54** 756 (2006).

[43] F.C. Coomer, A. Harrison, G.S. Oakley, J. Kulda, J.R. Stewart, J.A. Stride, B. Fak, J.W. Taylor, and D. Visser. J. Phys.: Cond. Matt. **18** 8847 (2006).

[44] J. Yang, New J. Phys. **6**, 47 (2004).

[45] J. Yang, A. Bezryadina, I. Makasyuk, and Z. Chen, Stud. Appl. Math. **113**, 389 (2004).

[46] H. Susanto, K. Law, P.G. Kevrekidis, L. Tang, C. Lou, X. Wang, and Z. Chen, Physica D **237**, 3123 (2008).
[47] C. T. Kelley, *Solving Nonlinear Equations with Newtons Method*, no. 1 in Fundamentals of Algorithms, SIAM, Philadelphia, 2003.
[48] E. Doedel. International Journal of Bifurcation and Chaos. **7**, 2127 (1997).
[49] T. Kapitula, P.G. Kevrekidis, and B. Sandstede, Physica D **195** 263 (2004).
[50] J.-C. van der Meer, Nonlinearity **3**, 1041 (1990).
[51] D. Pelinovsky, A.A. Sukhorukov, and Yu.S. Kivshar, Phys. Rev. E **70**, 036618 (2004).
[52] Z. Shi and J. Yang, Phys. Rev. E **75**, 056602 (2007).